Properties of Electron Distributions in the Martian Space Environment

G. Andreone, J. S. Halekas, D. L. Mitchell, C. Mazelle, J. Gruesbeck

JGR Space Physics

RESEARCH ARTICLE
10.1029/2021JA029404

Properties of Electron Distributions in the Martian Space Environment

G. Andreone[1], J. S. Halekas[1], D. L. Mitchell[2], C. Mazelle[3], and J. Gruesbeck[4]

[1]University of Iowa, Iowa City, IA, USA, [2]Space Sciences Laboratory, University of California, Berkeley, CA, USA, [3]IRAP/CNRS, University of Toulouse-UPS-CNES, Toulouse, France, [4]Goddard Space Flight Center, Greenbelt, MD, USA

Key Points:

- Solar wind electron analyzer aboard Mars atmosphere and volatile environment provides measurements of electron properties which provides insight into how the Martian space environment is organized
- Electron instruments suffer contamination in low energy measurements which must be removed to calculate correct temperatures and densities
- Different properties of electron distributions tells how electrons are heated as they cross the Martian bow shock and reveal instabilities

Correspondence to:
G. Andreone,
gian-andreone@uiowa.edu

Citation:
Andreone, G., Halekas, J. S., Mitchell, D. L., Mazelle, C., & Gruesbeck, J. (2022). Properties of electron distributions in the Martian space environment. *Journal of Geophysical Research: Space Physics*, *127*, e2021JA029404. https://doi.org/10.1029/2021JA029404

Received 2 APR 2021
Accepted 6 DEC 2021

Abstract Electron and magnetic field measurements from the Mars atmosphere and volatile environment (MAVEN) mission are utilized to study the interaction between Mars and the solar wind. Instruments like the solar wind electron analyzer (SWEA) aboard MAVEN measure properties of the electron environment over a broad range of electron energies. Measurements at low electron energies include contributions from spacecraft photoelectrons and secondary electrons that must be accounted for to accurately characterize the environment. We developed an algorithm to identify and remove secondary electron contamination to improve estimates of electron densities and temperature. We then compiled global maps of average electron density, temperature, and temperature anisotropy under different conditions, considering quasi-parallel and quasi-perpendicular bow shocks and upstream solar wind Alfven Mach number. Higher temperature anisotropy is observed for quasi-perpendicular shock crossings, as expected. We find significant electron temperature anisotropy upstream of the bow shock for quasi-perpendicular shock crossings, suggesting a heating mechanism, such as that provided by electromagnetic waves. We analyzed the influence of hi and low Alfven Mach number conditions and found the electron plasma beta to be the only electron property significantly affected. We studied the relationship between the electron distribution function and the generation of instabilities and conclude that the upstream Alfven Mach number influences the stability of electron distributions in the Martian environment.

Plain Language Summary Studying how the solar wind which flows from our sun interacts with Mars can give great insight into how Mars went from a warm, wet planet to a cold dry one over several billion years. An important part of this investigation is looking at the near-Mars space environment and how the solar wind traverses this environment to deposit energy into the upper Martian atmosphere. Electron properties often dictate the structure and variability of the planetary space environment. In this work, we utilize electron measurements from around Mars to understand how electron temperature and density affect this space environment. We also look at how unstable electron populations can transfer energy between particle populations and electromagnetic waves. However, instruments that measure electrons tend to have a significant amount of contamination in low energy measurement bins. Thus, a new algorithm is proposed to remove one source of contamination (secondary electrons from instrument and spacecraft surfaces), which leads to more accurate measurements of electron density and temperature.

1. Introduction

The terrestrial space environment provides a way to study how a flowing plasma interacts with a highly magnetized obstacle, which contrasts the intrinsically unmagnetized Martian space environment, an excellent laboratory to study the interaction between an intrinsically unmagnetized obstacle (Mars) and a supersonic magnetized plasma (the solar wind and the interplanetary magnetic field or IMF). While Mars has a bow shock, magnetosheath, and a magnetic pileup boundary just like Earth (Bertucci et al., 2012; Crider et al., 2004; Dubinin et al., 2007, 2008; Mazelle et al., 2004), the lack of a global intrinsic magnetic field combined with crustal fields complicates the interaction considerably. The Martian bow shock is pushed closer to the planet, leading to a significantly smaller magnetosheath than at earth. Moses et al. (1988) predicted that since the ion gyroradius is nearly equal to the size of the martian magnetosheath, the ion distribution cannot fully thermalize. The same argument cannot be made for observed non-thermal electron distributions since electrons have a significantly smaller gyroradius than ions. J. J. Mitchell and Schwartz (2014) developed a model which suggested that the non-thermal electron distributions are influenced by electron distributions at different positions on the bow shock. Understanding how these distributions evolve from the upstream solar wind down into the Martian atmosphere is crucial in understanding how Mars went from a warm, wet planet in the past to a cold, dry planet currently. How the solar wind evolves

from upstream of the bow shock to the magnetosphere helps in understanding how energy is transferred from the solar wind into the upper atmosphere and is ultimately capable of stripping Mars of its upper atmosphere. A recent study by Xu et al. (2021) looked at how electrons establish a cross-shock potential across the bow shock. Understanding how the ions are decelerated by this potential gives insight into how the solar wind ram energy is converted into thermal energy, and how these heated ions can participate in the pickup process thought to be responsible for degrading the upper Martian atmosphere.

There have been many investigations of Mars in the past, from Mariner-4 and Phobos-2, to present-day missions like Mars Global Surveyor and Mars Express. Recently, the Mars atmosphere and volatile environment (MAVEN) spacecraft (Jakosky et al., 2015) were placed in orbit around Mars to study the upper Martian atmosphere and how external drivers (like the solar wind) affect its evolution. A crucial component of this is understanding how the upstream solar wind and IMF control the planetary bow shock and properties of the magnetosheath. The ion population has been studied by Halekas et al. (2017), who found that both solar wind speed and IMF orientation with respect to bow shock surface (quasi-parallel vs. quasi-perpendicular) control the shape of the bow shock and ion temperatures in the magnetosheath. To complete the physical picture, it is important to study the analogous electron properties as well to understand the microphysics occurring in the Martian near-space environment.

There have been a few studies of electrons in the terrestrial magnetosheath (Lu et al., 2011; Masood & Schwartz, 2008) which showed that electron temperature anisotropy develops downstream of the bow shock. These studies have also shown that ions are heated more than electrons. J. J. Mitchell and Schwartz (2014) suggested that the overall electron distribution function is a combination of electron distributions originating at different locations on the bow shock, meaning overall electron properties in the sheath are affected by global (rather than local) factors. Schwartz et al. (2019) applied this model to Martian magnetosheath electrons and was able to reproduce important features of the distribution, suggesting that these electron populations are also affected by global effects. Fränz et al. (2006) calculated various moments of the distribution function and showed global maps of electron density and temperature in the magnetosheath. These maps showed that electron density and temperature are largest near the subsolar point of the bow shock, suggesting this is where the solar wind is most compressed downstream of the shock. This study also showed that ions are heated more than electrons downstream of the bow shock. We take this a step further by looking at temperature anisotropies with respect to the magnetic field and how these can drive instabilities in the Martian space environment.

Charged particle instruments, such as the solar wind electron analyzer (SWEA) (D. L. Mitchell et al., 2016), suffer from contamination in low energy measurements, especially in regions with hot flowing plasma. This is due to suprathermal electrons striking various spacecraft and instrument surfaces to produce low energy secondary electrons, which leads to overestimates of electron density and underestimates of electron temperature components. We developed an approach to model the secondary electron spectra and iteratively remove them from the primary spectra. This leads to better agreement between electron and ion densities in the sheath as well as improved temperature measurements.

2. MAVEN Observations and Data Correction

2.1. MAVEN Observations

Electron measurements in the Mars environment were made by SWEA (D. L. Mitchell et al., 2016). SWEA is a hemispherical electrostatic analyzer capable of measuring electrons from 3eV-4 keV. Since MAVEN does not spin, SWEA utilizes electrostatic deflectors to direct electrons from different angles onto 16 detectors (”anodes”) each spanning 22.5° to provide 360 degrees of the circular target area. The electrostatic deflectors select a particular look direction by applying different voltages to the curved conducting surfaces of the deflectors to achieve a field of view (FOV) of 120,360°. The combined energy and angular coverage of SWEA allows a nearly complete sampling of the electron distribution function in the magnetosheath and solar wind. Fully calibrated 1 s magnetic field measurements, provided by the MAVEN magnetometers (Connerney et al., 2015), are utilized to organize the charged particle data sets and to separate measurements of temperature into parallel and perpendicular components with respect to the magnetic field. Finally, complimentary solar wind ion measurements, provided by the solar wind ion analyzer (SWIA) (Halekas et al., 2015), were utilized both as a metric for determining how well the secondary correction worked and to give context to the electron measurements.

Before moving on, one must be aware of the problems which occur with electron measurements. The first main issue is low energy contamination due to externally produced photoelectrons from the spacecraft and both internally and externally produced secondary electrons. Removing this contamination takes some care, as will be discussed in the next section. The second major issue deals with spacecraft charging effects. As MAVEN travels through the magnetosheath in sunlight, it charges positively to offset the photoelectron loss caused by EUV photons striking the spacecraft surface. To correctly calculate bulk moments of the distribution function, this spacecraft potential needs to be taken into account (discussed in Lavraud & Larson, 2016).

The third major issue is a consequence of SWEA's incomplete FOV. As stated earlier, SWEA utilizes electrostatic deflectors to compensate for the fact that MAVEN does not rotate. This results in time periods where the magnetic field lies outside the FOV. This means important science results, such as temperature components with respect to the magnetic field and loss cones, are not completely measured for some magnetic field orientation. This study only utilizes electron distribution function measurements where the magnetic field was in the SWEA FOV.

2.2. Secondary Electron Correction

Low energy contamination in electron distribution measurements (electrons with energies less than 20 eV from both spacecraft photoelectrons and secondary electrons) has been observed previously in electrostatic analyzers (e.g., McFadden et al., 2008). When a spacecraft is exposed to EUV radiation from the sun, photoelectrons are ejected from the spacecraft, causing it to charge positively. To account both for the shift in ambient electron energy due to this positive charging and eliminate most of the spacecraft photoelectron contamination, we can calculate the spacecraft potential ϕ_{sc}, below which most of the photoelectron population resides. Electron spectra often show a clear demarcation between the photoelectrons and other electron populations. For the rest of this manuscript (except in Figure 5), spacecraft photoelectrons have been removed from the spectra used and spacecraft charging has been taken into account

Secondary electron contamination (electrons ejected when a high energy electron impacts an instrument or spacecraft surface) proves more difficult to remove since the population is a function of the instrument and spacecraft itself, and can overlap the primary population in energy. The interaction of energetic electrons with metal surfaces has been well documented, both experimentally and theoretically (Bouchard & Carette, 1980; Scholtz et al., 1996). Using two assumptions about the secondary electron population, we aim to calculate an approximation of the secondary electron spectrum. The first assumption (deduced from SWEA measurements) is the total number of secondaries produced is directly correlated to the temperature of the ambient electron population. Thus a hotter plasma will produce more secondaries (which occurs in the Martian magnetosheath). This assumption is implemented in our algorithm through the secondary electron yield function, which quantifies how likely ambient electrons are at liberating secondary electrons from a given surface. The second assumption is that the shape (how wide and where the peak energy is located, quantified through the secondary shape function S[E]) of the secondary spectrum depends only on the material of the surfaces emitting the secondaries (this assumption ignores backscattered electrons).

We developed an algorithm to remove secondary electron contamination from measured electron spectra. The total number of secondary electrons produced given an ambient plasma population at a certain temperature should be proportional to the total ambient differential electron flux $\mathrm{F} = \int_{E_{e\phi_{sc}}}^{E_{\max}} F_E(E')dE'$, which is the total flux obtained by integrating the differential electron flux F_E over energy. However, this expression should be modified since electrons at certain energies are more efficient at producing secondary electrons than other energies. The yield is a measure of this efficiency so the modified total flux is $\mathrm{F} = \int_{E_{e\phi_{sc}}}^{E_{\max}} F_M(E')\delta(E')dE'$. Then the secondary differential electron flux is $F_s = \epsilon\ \mathrm{F}\ \mathrm{S(E)}$, where epsilon is the free parameter in the presented algorithm and is a representation of how well we chose the yield. The functional form of S(E) is chosen so that $\int_{E_{e\phi_{sc}}}^{E_{\max}} S(E')dE' = 1$ (normalized to unity). The overall approach taken is to make an initial guess for the secondary differential electron flux F_s and subtract it from the original measured differential electron flux F_M to give an initial guess for the ambient differential electron flux F_a. This approach is repeated, adjusting F_s until F_M is sufficiently close to $F_{Mnew} = \mathrm{F}_m + \mathrm{F}_s$. Note that all differential electron fluxes used in the algorithm are functions of energy. We used a yield with a peak at 300 eV, which was decided upon after implementing the algorithm with different peak yield energies and determining which separated the ambient and secondary spectra most cleanly. SWEA measurements

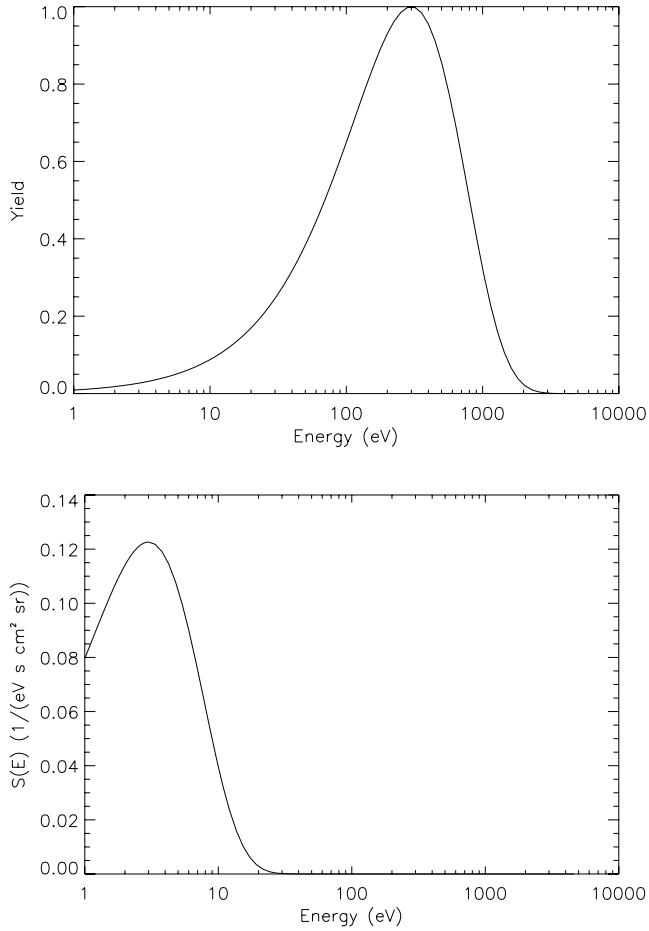

Figure 1. $\delta(E)$ (top) and S(E) (bottom). As stated, the yield is peaked at 300 *eV*.

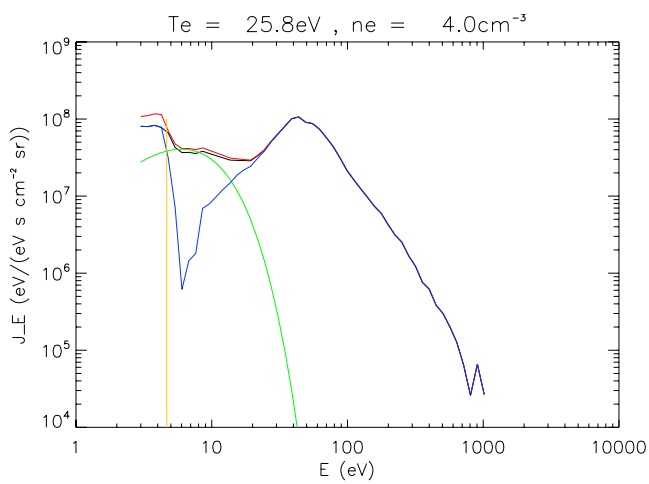

Figure 2. Sample electron spectra in the magnetosheath, decomposed as follows: Originally measured spectra (black), New measured spectra F_{Mnew} (red), Ambient plasma spectra (blue), Secondary electron spectra (green), and ϕ_{sc}.

of F_E suggest the secondary electron spectra in this case have a peak at 3 eV and fall off very rapidly after 20 *eV*. The yield $\delta(E)$ and secondary shape function $S(E)$ used in the current study are shown in Figure 1.

The details of the algorithm we developed to separate secondary and ambient electron distributions works as follows:

1) Make an initial guess at an energy that provides an approximate separation between ambient and secondary populations (which is denoted by E_{cut})
2) Calculate

$$F_a = F_M - F_{0s} \tag{1}$$

where $F_{0s} = \epsilon S(E) \int_{E_{cut}}^{E_{max}} F_M(E')\delta(E')dE'$ is the initial guess for the secondary differential electron flux integrated from E_{cut}

3) Next calculate

$$F_{Mnew} = F_a + F_s \tag{2}$$

If $F_{Mnew} < F_M$ for all energies, then the algorithm has underestimated the secondary electron population and ϵ is increased. Otherwise, the algorithm has overestimated the secondary population and ϵ is decreased.

4) Next, Calculate

$$F_a = F_M - F_s \tag{3}$$

Where F_s, F_a, and F_m are defined in the previous paragraph

5) Repeat step 3 to calculate $F_{Mnew} = F_a + F_s$ and adjust the ϵ factor depending on whether the current secondary spectra is an over- or under-estimate of F_s
6) Repeat steps 4 and 5 until Max($|F_{Mnew} - F_M|$), the maximum difference between these two quantities, is below some threshold (for this study it was 10^3 $1/(eVcm^2srs)$)

An example of decomposed electron spectra is shown in Figure 2 and a time series of decomposed spectra is shown in Figure 3. Note that the algorithm has successfully removed the secondary electron population (the green curve) from the originally measured spectra (the black curve), but the photoelectrons are still present. However, calculating bulk moments of the distribution function can easily exclude photoelectrons. This is done by excluding SWEA measurements with energies below $e\phi_{sc}$, as well as shifting all measurements above $e\phi_{sc}$ by the appropriate amount.

The blank regions in the secondary spectra shown in Figure 3 are locations where no correction is necessary or not appropriate (this will be elaborated on at the end of this section).

An important metric to determine how well the correction algorithm works is comparing electron and ion densities. Assuming quasi-neutrality in the Martian space environment (which is a reasonable assumption in most space plasmas), the electron and ion densities should be equal. Figure 4 shows a time series of the electron densities measured by SWEA and ion densities measured by SWIA. Comparing the electron densities (black points) and ion densities (red points) before (right) and after (left) the correction shows

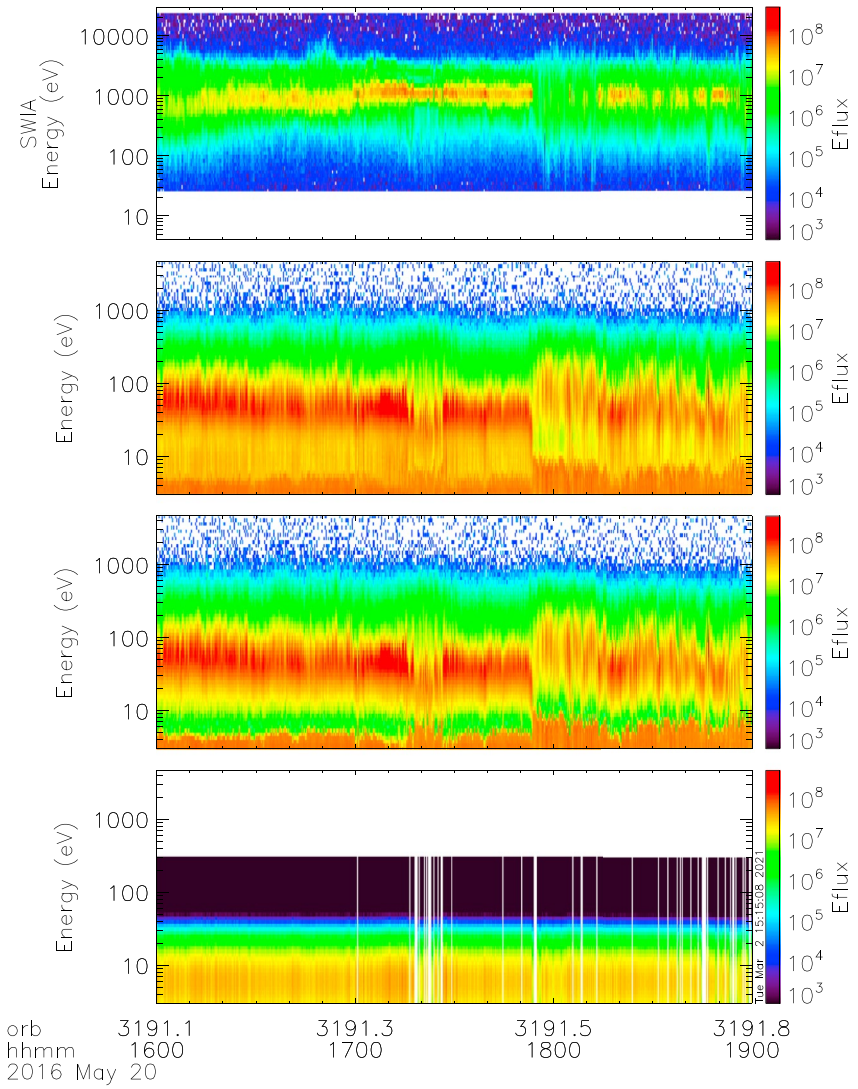

Figure 3. Solar wind ion analyzer differential energy flux (top), Original Measured solar wind electron analyzer spectra (second panel), corrected ambient spectra (third panel), secondary spectra (fourth panel). All EFLUX units are eV/(eV s sr cm^2) and photoelectrons have not been removed from the spectra.

better agreement post-correction. The average electron temperatures on the bottom panels also show an increase post-correction, since a low energy portion of an electron distribution is removed. Since plasmas in space rarely deviate from quasi-neutrality, the remaining discrepancies between ion and electron densities are due to instrument limitations, such as incomplete FOV measurements for both SWIA and SWEA, as well as the energy range for ion measurements (the minimum ion energy measured by SWIA is 15 *eV*). The inability of SWIA to differentiate between different ionic species can also lead to issues in calculating the total ion density.

While the above algorithm was originally developed for omni-directional spectra, it is readily extended by applying the algorithm to each look direction of the electron instrument. For SWEA, there are 96 total look directions so the algorithm is applied 96 times. Figure 5 shows an example of a 2-dimensional slice of the full 3-dimensional distribution function, which is plotted so the magnetic field points out of the plot. Note that the corrected spectra are gyrotropic with respect to the magnetic field, which makes sense since the electrons are highly magnetized.

Finally, it is interesting to see what the secondary electron correction does to the spatial distribution of densities in the Martian space environment. Figure 6, which shows the ratio of pre-corrected to post-corrected densities and average temperatures, demonstrates that near the sub-solar point, the correction is most significant. This

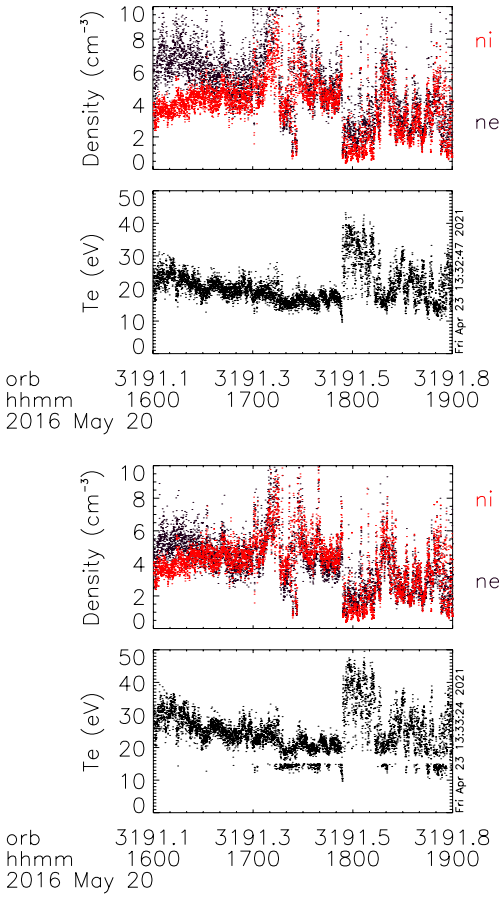

Figure 4. Uncorrected (top) and corrected (bottom) moments of the distribution function. The top panels show both electron (black points) and ion (red points) densities, while the bottom panels show average electron temperature before and after correction.

makes intuitive sense since the solar wind is most compressed and heated near the subsolar point, and gradually loses energy farther away. This means that substantial secondary contamination is more likely in this region than the flanks of the magnetosheath. The bottom two plots of Figure 6, which are electron density and average temperature (normalized to upstream solar wind ion density and temperature, respectively) also show good agreement with the results of Fränz et al. (2006) who showed substantial electron compression and heating near the subsolar point.

While the algorithm presented in this section works well when dealing with hot plasma, some caveats need to be mentioned. First, unless explicitly told not to, the algorithm will attempt to remove a portion of the low energy population even when the secondary population is negligible (such as in the solar wind and ionosphere). This is dealt with by not performing the correction if the maximum temperature is too low ($<15\ eV$ for this study). It is also important to note that this correction would not work in regions where ion and electron analyzers are not capable of measuring the bulk of the plasma spectra (e.g., the ionosphere of Mars where the bulk of the plasma population lies below the minimum energy thresholds of both SWEA and SWIA). With these caveats in mind, corrected electron spectra measured in the Martian space environment can be used to calculate global electron properties and the ability of these spectra to induce instabilities, as will be discussed in the next section.

3. Results

3.1. Averaged Electron Properties for Different Solar Wind Conditions

To understand how the solar wind interacts with an unmagnetized obstacle (such as Mars), we look at spatial maps of average electron properties for a variety of solar wind conditions. Solar wind properties (such as ion temperature and density) upstream of the bow shock were obtained through SWIA (Halekas et al., 2017). Maven has an orbit which processes around Mars with an orbital period of 4 hr leading to periods of time when the spacecraft would not cross into the solar wind. During these times it is difficult to infer solar wind properties, so the data were filtered so that only measurements taken within 8 hr of MAVEN crossing into the solar wind were used, as well as by those times when the magnetic field was within the SWEA field of view. A useful coordinate frame to study these properties is the Mars-Sun-Electric (MSE) frame, where the x-axis is pointed toward the sun, the z-axis is in the direction of the solar wind convective electric field ($E_{sw} = -u_{sw} \times B_{imf}$), and the y-axis completes the coordinate triad. The benefit of using this frame is that B_{imf} is entirely in the x-y plane and always has a positive y-component. This means that filtering data based on IMF cone angle (the angle between the IMF direction and X_{MSE}) can separate quasi-parallel from quasi-perpendicular bow shock crossings. In particular, for cone angles from 0° to 60°, quasi-perpendicular crossings correspond to $Y_{MSE} < 0$ and quasi-parallel crossings correspond to $Y_{MSE} > 0$, whereas those distinctions are switched for cone angles from 120° to 180°. The data are binned into 400 km bins. We also filter so we only use data where $|Z_{mse}| \leq 2000$ km, in order to clearly show the bow shock and magnetosheath properties in the B-V_{sw} plane. Finally, electron density and temperature measurements are normalized to upstream ion density and temperature components, respectively.

Figure 7 shows data for different IMF orientations. First, the bow shock and magnetosheath are organized by the IMF, as expected based on gas-dynamic simulations. Electron density, n_e, tends to be symmetric with respect to IMF orientation and as stated before is higher near the subsolar point on the bow shock than the flanks since the solar wind is most compressed at this location. Electron temperature components on the other hand (both $T_{e\perp}$ and $T_{e\parallel}$) tend to be mildly organized by IMF direction with respect to the bow shock normal. $T_{e\perp}$ is larger for quasi-perpendicular shock crossings (for cone angles from 120° to 180° this corresponds to $Y_{MSE} > 0$ while cone angles from 0° to 60° corresponds to $Y_{MSE} < 0$). The opposite occurs for $T_{e\parallel}$, suggesting the development of temperature anisotropies which will be discussed next.

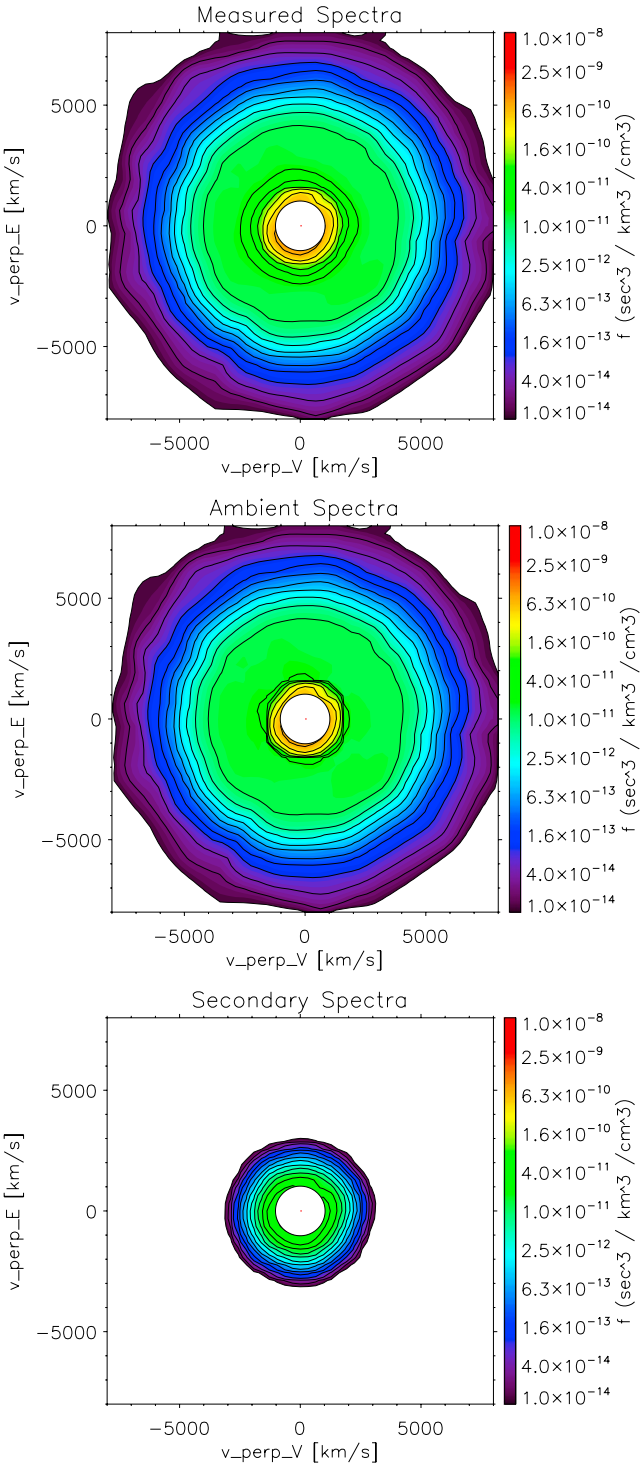

Figure 5. 3-Dimensional spectra decomposed into measured, ambient, and secondary spectra. The axis is oriented so the magnetic field points out of the page. The corrected (ambient) spectra are gyrotropic around the magnetic field, as is expected due to the highly magnetized nature of the electron distribution.

The most striking features of filtering data based on IMF orientation with respect to the bow shock show up in the temperature anisotropy (T_{perp}/T_{para}) (Figure 8), with greater anisotropy occurring for quasi-perpendicular crossings. Electron temperature anisotropy is often an indicator of how capable the electron distribution is at driving instabilities (as will be elaborated on in the next section). These instabilities help dictate how energy and momentum are transferred between the plasma and electromagnetic waves. A specific example demonstrating some interesting instabilities is the case when the data is filtered by cone angles in the range of 120°–180°. In the quasi-perpendicular region ($Ymse > 0$) there is not only enhanced temperature anisotropy in the magnetosheath, but also in the upstream solar wind. This is very interesting since electrons are highly magnetized (small gyro-radii means they convect through the magnetosheath along the magnetic field) and are therefore very unlikely to be reflected into the upstream solar wind in the quasi-perpendicular region. However, previous studies (Mazelle et al., 2018) did show an anisotropic energetic electron distribution upstream of nearly-perpendicular bow shock crossings. Significant temperature anisotropies upstream of the bow shock are not seen in ion observations (Halekas et al., 2017). Wave activity has been observed upstream of the bow shock for example, Ruhunusiri et al. (2018). Ions have a gyroradius comparable to the size of the Martian magnetosheath. This causes the formation of an ion foreshock upstream of the bow shock capable of driving waves. Whistler waves were among those observed upstream of the bow shock, which can energize electron populations. Future investigations are needed to determine if electron temperature anisotropy upstream of the bow shock is a cause or consequence of these whistler waves, as well as how efficient this whistler wave heating is compared to other mechanisms, like Fermi acceleration.

To understand why these temperature anisotropies occur, it's important to consider the conservation of adiabatic invariants (as derived from the model of Chew et al., 1956). The first invariant derives from conservation of magnetic moment ($\frac{T_\perp}{B} = const$) while the second derives from conservation of angular momentum ($\frac{T_\parallel B^2}{\rho^2} = const$). While the conservation of adiabatic invariants traditionally relies on the assumption of a thermal (Maxwellian) distribution, these invariants can give a qualitative picture of why anisotropies develop. Combining the two adiabatic invariant relations, one gets $\frac{T_\perp}{T_\parallel} = \left(\frac{\rho_{sw}}{\rho}\right)^2 \left(\frac{B}{B_{sw}}\right)^3 \left(\frac{T_{\perp sw}}{T_{\parallel sw}}\right)$, where B and ρ correspond to the downstream (magnetosheath) magnetic field and mass density, while B_{sw} and ρ_{sw} correspond to the analogous upstream (solar wind) values. For quasi-perpendicular shock crossings, the increased (compressed) magnetic field has a higher field strength, causing the electrons to gyrate faster around the magnetic field line, leading to more perpendicular than parallel heating. For parallel shock crossings, there is a greater increase in the parallel temperature than perpendicular, but the increase is smaller. However, the ions showed much more substantial heating in both quasi-parallel and quasi-perpendicular bow shock crossings (Halekas et al., 2017) and a clearer organization for the bow shock. The fact the electron distribution shows substantially less increase in $T_{e\perp}$ and $T_{e\parallel}$ separately suggests that the non-local nature of the distribution function affects these properties, as modeled by Schwartz et al. (2019).

Next, spatial data is organized based on the upstream solar wind Alfven Mach number M_A (Figure 9). Unlike the ions (Halekas et al., 2017), the electrons do not exhibit as much heating. This makes sense since the majority of the converted solar wind ram energy is distributed to the ions. However, Figure 10

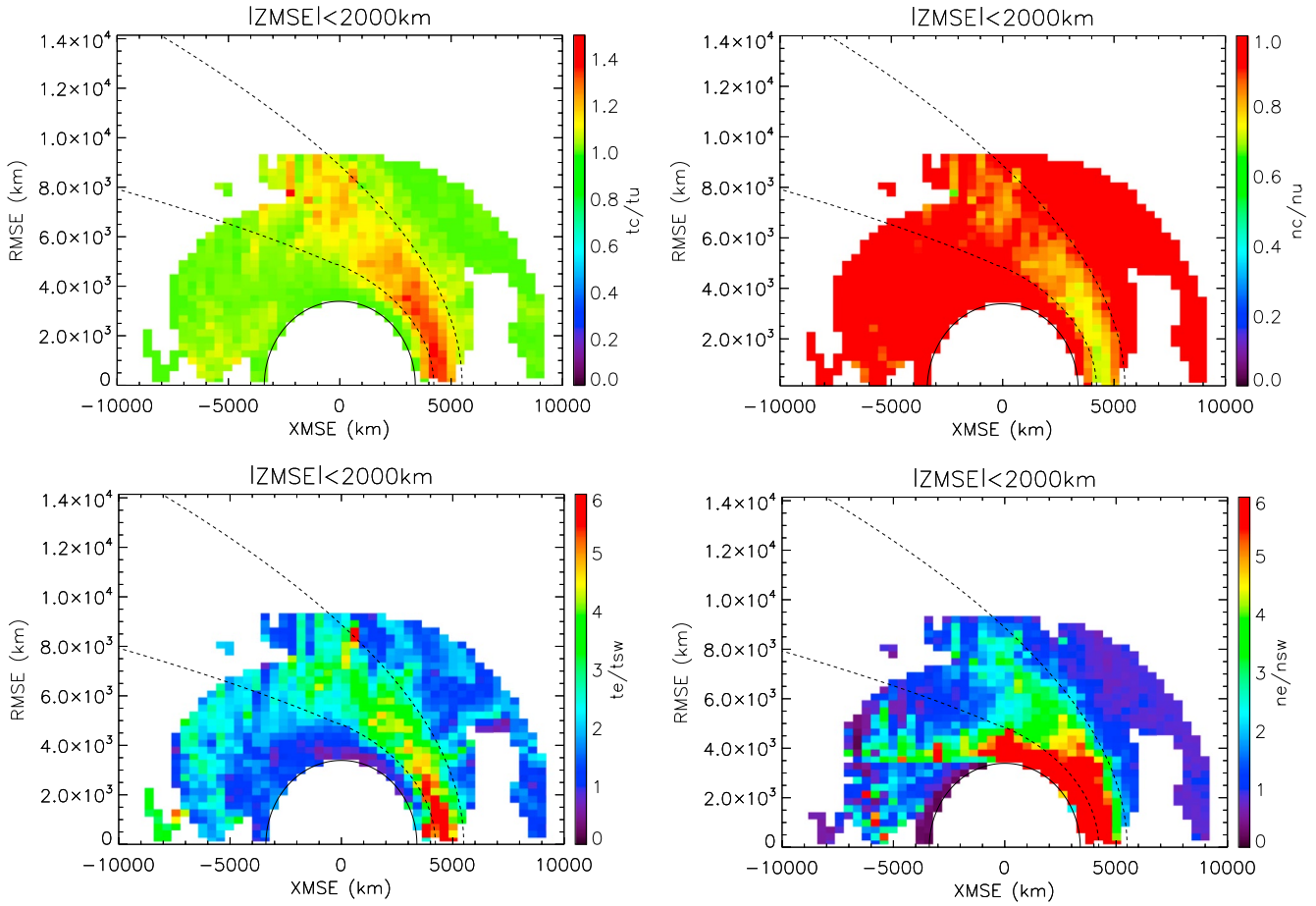

Figure 6. Top: $\frac{n_c}{n_u}$ and $\frac{t_c}{t_u}$ (the ratio of corrected to uncorrected density and average temperature, respectively) averaged over two years of solar wind electron analyzer data (2017 and 2018). Bottom: n_e and T_{eavg} normalized to solar wind density and temperature, respectively. Note that electron densities will be underestimated when Mars atmosphere and volatile environment is in the Martian shadow, since the spacecraft has a negative potential.

shows that electron beta significantly increases with increasing M_A. Dimmock et al. (2015) showed that lower M_A leads to lower ion plasma beta and higher ion temperature anisotropy in the terrestrial magnetosheath. Halekas et al. (2017) showed the same thing for ions downstream of the Martian bow shock. It's interesting that electron temperature anisotropy isn't more controlled by electron plasma beta. It would be expected that any electron temperature-anisotropy would die out very quickly due to higher electron beta. In the next section, the question of instabilities driven by electrons will be investigated.

It's informative to compare electron and ion heating downstream of the bow shock. Wang et al. (2012) utilized THEMIS measurements in the Terrestrial magnetosheath to compare electron and ion heating as the solar wind crosses the bow shock. This study showed that ions are heated more substantially than electrons. A similar comparison at Mars can be made by looking at the study by Halekas et al. (2017). Comparing the relative temperatures between the ions and electrons, the ions tend to be more heated than electrons after crossing the bow shock. These observations match those made at Earth, which suggests that despite the large size difference between the Terrestrial and Martian magnetosheaths, they share some very similar features. Also the ions show greater temperature anisotropies than electrons so both electrons and ions are capable of driving instabilities in the Martian space environment

The above results have shown that varying solar wind and IMF conditions can greatly affect the Martian space environment. This then leads to the questions of how the shocked solar wind can potentially drive instabilities in this same environment, and how these instabilities can then affect upstream and downstream plasma populations. The next section looks at the potential for these instabilities to form.

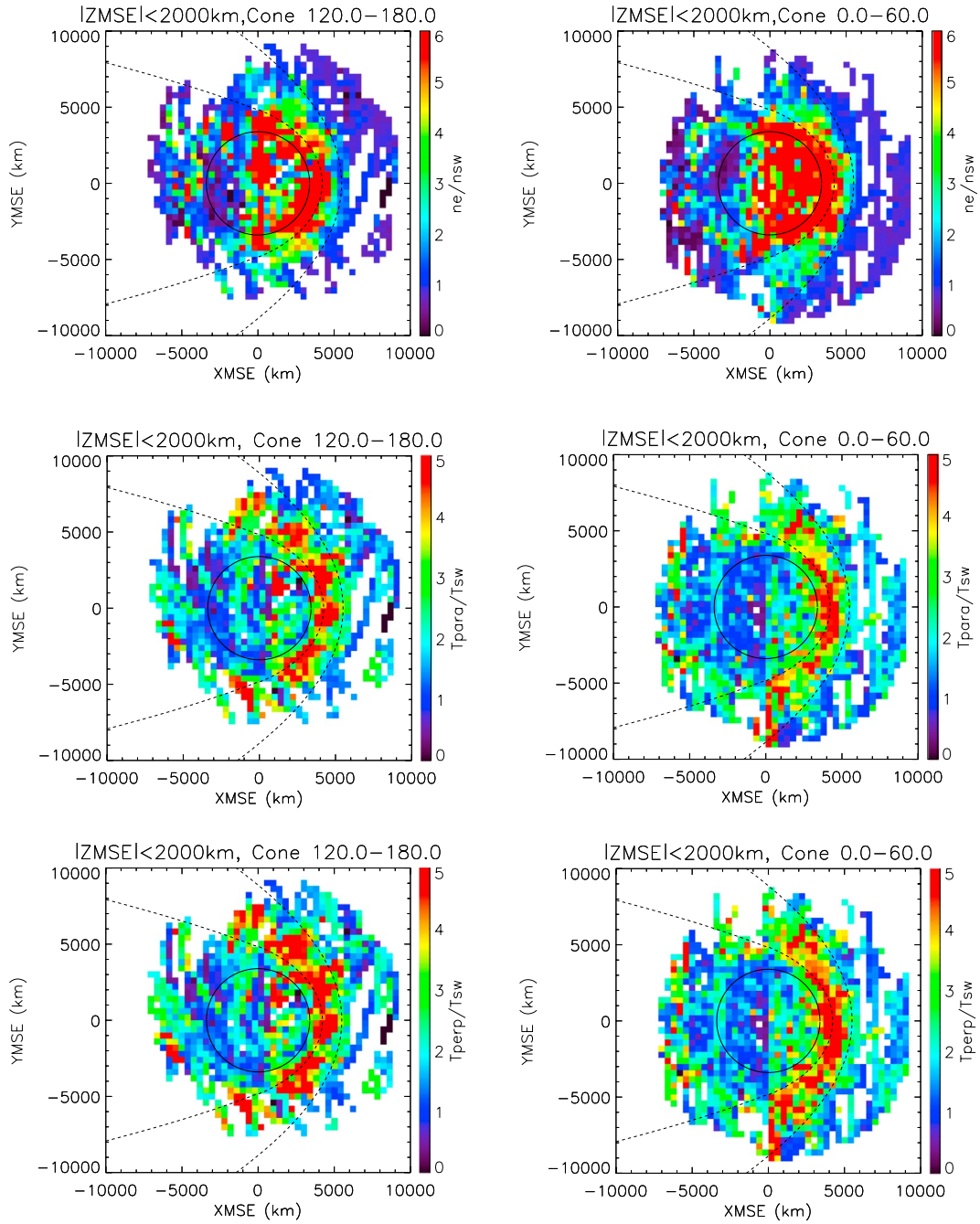

Figure 7. Electron properties for $B_{imfx} < 0$ (left) and $B_{ximf} > 0$ (right). Top row is n_e, the middle row is $T_{e\|}$ and bottom row is $T_{e\perp}$ which are all normalized to upstream solar wind conditions.

3.2. Instabilities in the Martian Space Environment

Certain combinations of electron temperature anisotropies and high electron plasma beta values drive a variety of plasma instabilities. Štverák et al. (2008) studied how capable electron distributions are of being driven unstable in the solar wind and showed that electron distributions are stable and away from instability limits. There was also a study in the Terrestrial magnetosheath (Gary et al., 2006) which placed constraints on electron temperature anisotropy based on the ability for electron distributions to drive instabilities. However, no similar studies have been performed at Mars. Figure 11 plots electron temperature anisotropy against electron beta.

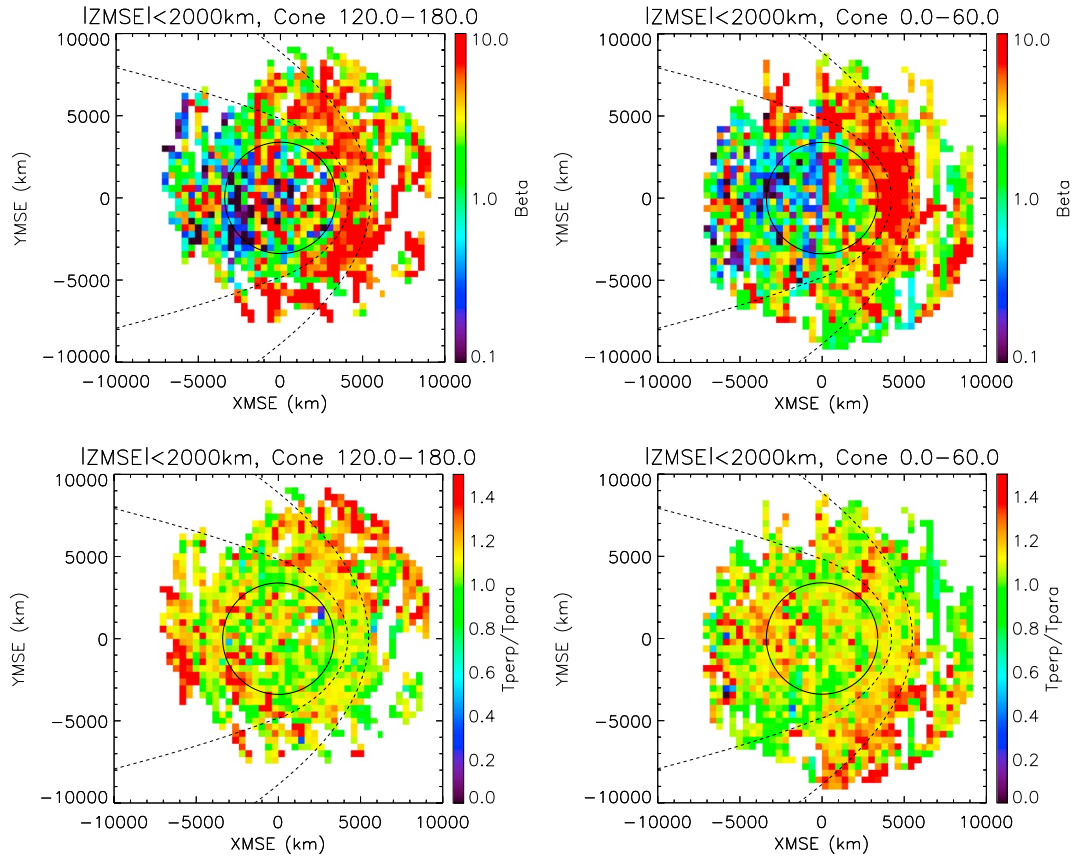

Figure 8. Derived fluid and kinetic electron properties based on interplanetary magnetic field orientation relative to the bow shock normal.

The white curves indicate instability thresholds, with the top one representing the whistler-mode instability, while the bottom is the firehose instability. The whistler-mode instability threshold (which was derived by Gary & Nishimura, 2003) is a kinetic instability occurring in magnetized plasmas, which is more likely to occur with a higher temperature anisotropy. The instability begins to grow when electrons resonate with the electric field component of an electromagnetic wave transverse to the background magnetic field, allowing the transfer of energy between the wave and the plasma population. The firehose instability (derived by Gary & Wang, 1996), on the other hand, is a fluid instability. This instability is more likely to grow with lower temperature anisotropy and is associated with substantial magnetic field perturbations relative to the background magnetic field.

Figure 12 shows electron temperature anisotropy versus electron plasma beta filtered by M_A. As stated in the previous section, the only electron property significantly affected by M_A is electron plasma beta. Figure 12 shows that as M_A increases upstream of the bow shock the entire electron population is moved closer to the instability thresholds. While the majority of electron distributions are constrained by the instability thresholds, it is interesting to note that higher M_A pushes the electron population up against the instability thresholds and appears to have a larger number of unstable electron distributions than lower M_A. This again points to the fact that non-local factors (such as M_A) affect the electron distribution at different locations in the sheath, while local factors act to stop the growth of instabilities.

It is important, however, to be aware of the assumptions that went into deriving the instability thresholds mentioned in the previous paragraphs. First, the thresholds were derived from the growth rates of the two instabilities mentioned (whistler-mode and firehose using linear plasma kinetic theory, which is valid during the initial onset of these instabilities). Eventually, linear theory becomes invalid and nonlinear effects begin to take effect, driving the electron population toward stability. Second, the thresholds were derived assuming a thermal Bi-Maxwellian distribution. While f_e is assumed to be gyrotropic around the magnetic field, it is not necessarily Bi-Maxwellian. Schwartz et al. (2019) showed that electron distributions broaden after crossing the bow shock, then evolve back

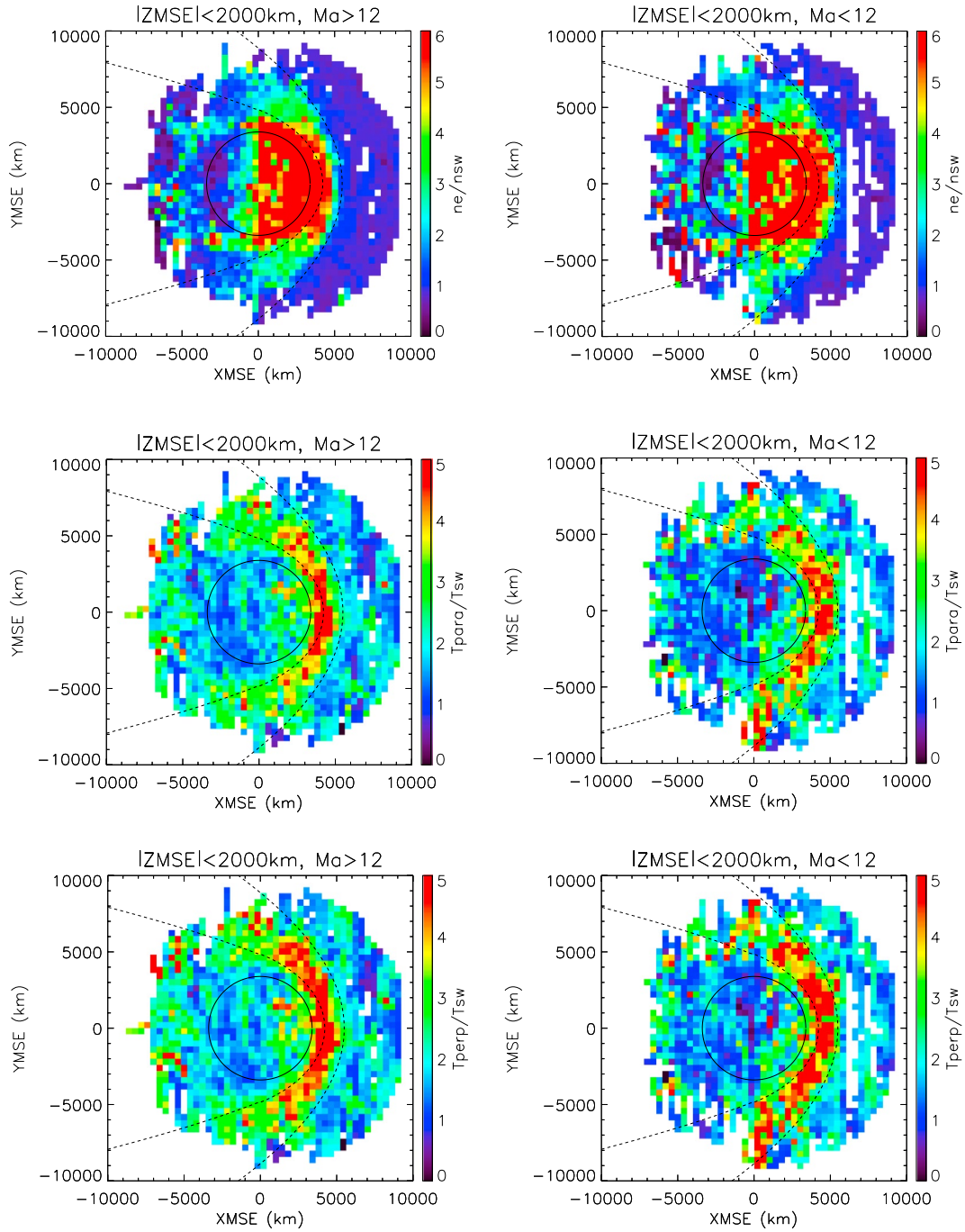

Figure 9. Electron properties based on low (left) and high (right) Alfven Mach number M_a.

to the pre-shocked upstream solar wind distribution deeper into the Martian magnetosheath. The growth rates used to calculate the instability thresholds are also very sensitive to the slope of f_e in places where electrons resonate with electromagnetic waves, where non-linear effects tend to be prominent. Since the growth rates depend on the actual shape of the electron distribution, and since a Bi-Maxwellian cannot be necessarily assumed, the thresholds used in this study may not be as well determined at Mars as they are in a different space environment (e.g., the solar wind). Finally, the thresholds are derived assuming a growth rate of $\Omega_{ce} \times 10^{-2}$, where Ω_{ce} is the electron cyclotron frequency. This growth rate may be slow compared to the time it takes for the upstream solar wind to traverse the bow shock, which could also lead to inaccurate calculations for the instability thresholds.

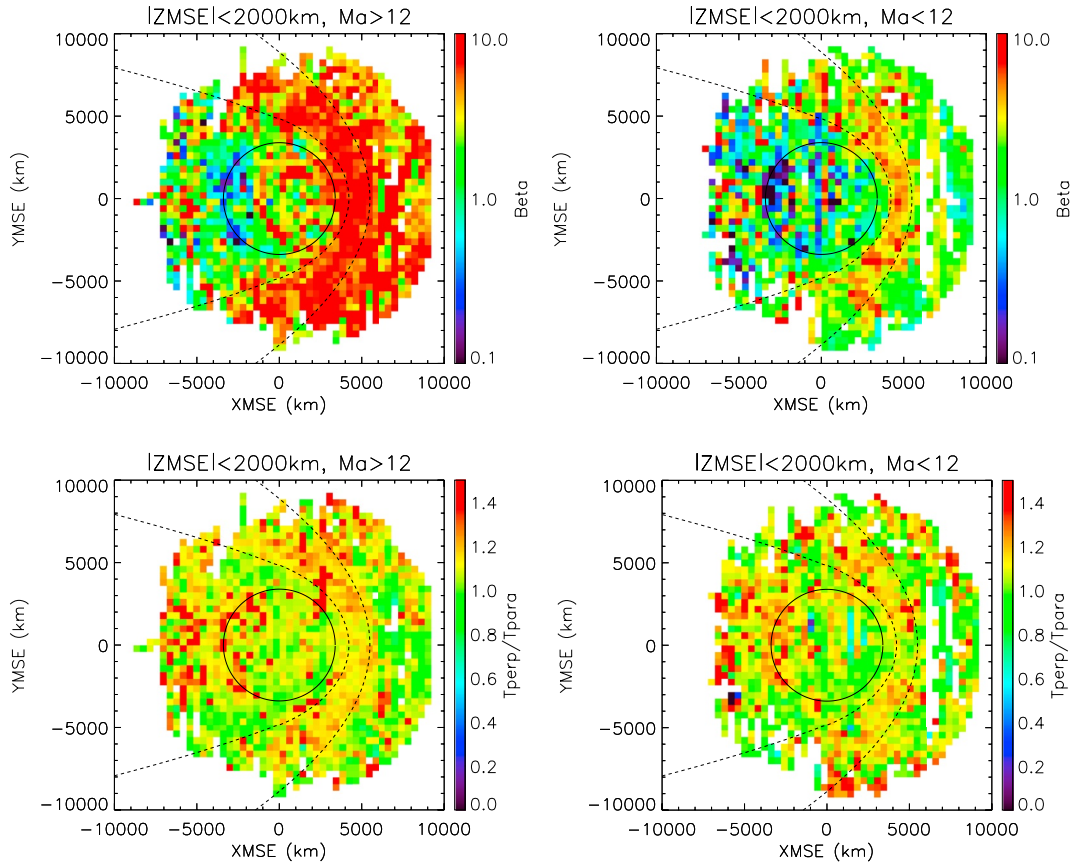

Figure 10. Derived fluid and kinetic electron properties based on high or low M_A.

4. Conclusion: Electrons at Mars

The Martian space environment provides an interesting laboratory to study how the solar wind interacts with an unmagnetized obstacle. In particular, electron distributions can provide insight into different physical characteristics of the Martian space environment, such as the cross-shock potential across the Martian bow shock, as

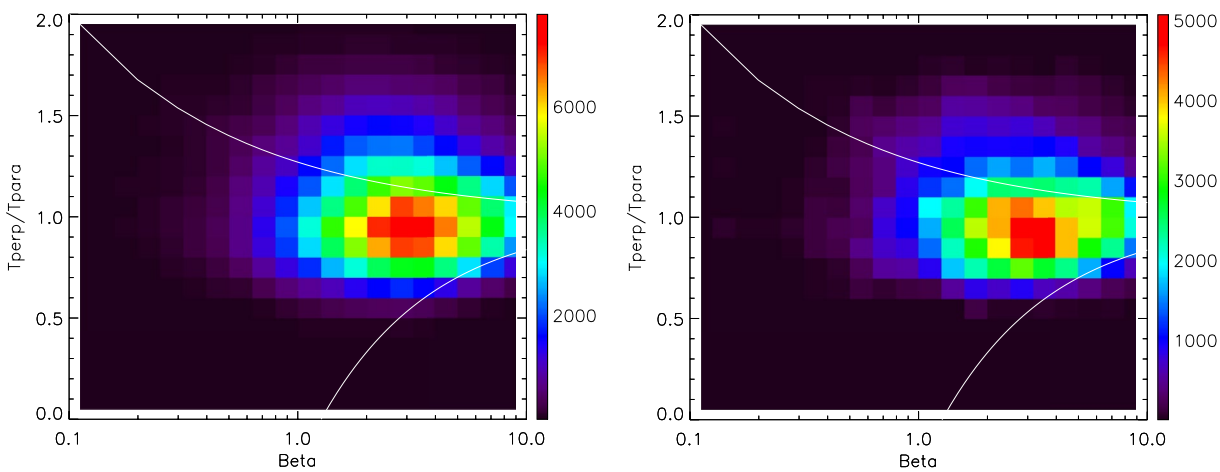

Figure 11. Electron temperature anistropy versus plasma beta in the Martian magnetosheath (left) and pristine solar wind (right). The color bar indicates the total number of points in each histogram bin. The top white curve (whistler mode threshold) is given by the relation $\frac{T_\perp}{T_\parallel} = 1 + \frac{0.27}{\beta^{0.57}}$, while the bottom white curve (firehose threshold) is given by $\frac{T_\perp}{T_\parallel} = 1 - \frac{1.23}{\beta^{0.88}}$, derived assuming a growth rate of $\Omega_{ce} \times 10^{-2}$. Unstable distributions are above the top curve and below the bottom curve.

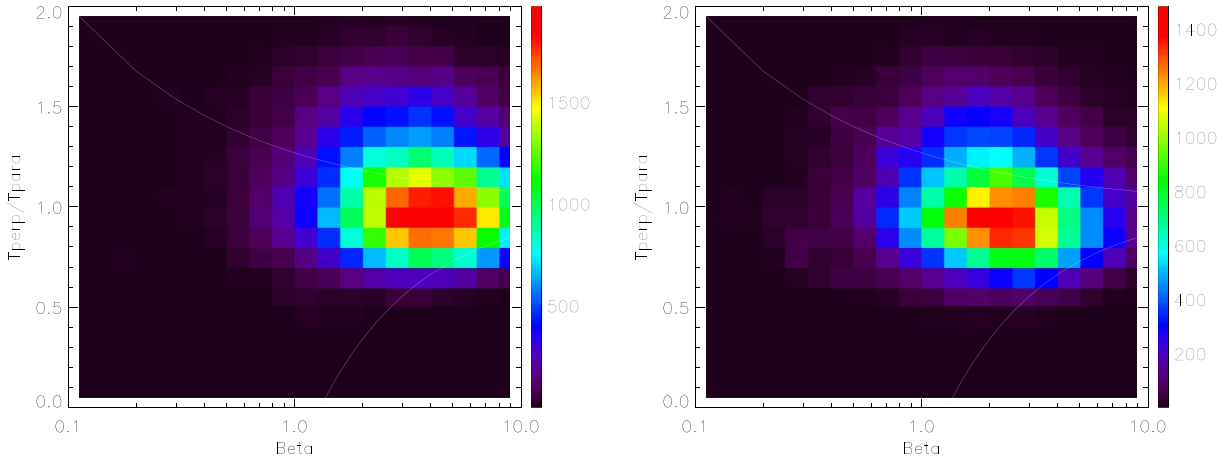

Figure 12. Electron instability plots in the Martian magnetosheath filtered by high (≥12) (right) and low (≤12) (left) M_A.

stated in the introduction. In this study, we saw that electron properties varied depending on solar wind and IMF properties. The bow shock was organized by quasi-perpendicular versus quasi-parallel bow shock crossings and electrons developed a higher temperature anisotropy for quasi-perpendicular shock crossings than quasi-parallel crossings. However, the presence of high temperature anisotropy upstream of the bow shock during quasi-perpendicular shock crossings suggests the presence of interesting wave phenomena, which could potentially result from the solar wind interacting with the Martian bow shock. Electron properties were also seen to be organized by M_A, and high M_A conditions showed a dramatic increase in electron beta, as expected. This suggests that any perturbation to the electron distribution function is quickly eliminated since electron instabilities are bounded by the aforementioned instability thresholds. This suggests that while global factors may be trying to drive anisotropies in the distribution (since the electron distribution is affected by global, rather than local, factors (Schwartz et al., 2019) local plasma instabilities are acting to suppress any large anisotropy.

We developed and validated an algorithm to remove low-energy secondary electron contamination from the measured electron spectra. This algorithm works well in hot plasma environments (like planetary magnetosheaths) and is essential to capture the kinetic physics of the magnetosheath plasma population. This algorithm could potentially be applied to other planetary missions (such as Venus Express) which measure suprathermal electron populations, and missions designed to study the solar wind (e.g., Parker Solar Probe). Near the Sun or during magnetic reconnection at planets, hot electron populations tend to strike both the spacecraft and charged particle instruments. As stated in the introduction, the production of secondary electrons tends to skew electron kinetic properties, which are crucial to understanding phenomena such as magnetic reconnection or solar wind heating near the sun.

Finally, we were able to compare Martian ions and electrons (using results from Halekas et al., 2017) and compare the relative heating of the two species after crossing the bow shock. We can see that the ions get the majority of the energy downstream of the shock. However, both electrons and ions are able to drive instabilities in the Martian space environment, which is important in understanding the overall thermodynamics of the Mars-Solar wind interaction. These observations also match similar observations made at Earth using THEMIS measurements. Since the magnetosheath is a tenuous region of non-thermal electron and ion distributions, it is remarkable that the terrestrial magnetosheath plasma shares many similarities with Mars.

Several future studies are utilizing the results from the present manuscript. Looking at specific instances of unstable electron distributions and any wave activity during those times can provide insight into microphysics occurring in the Martian space environment. Also looking at spatially where the unstable distributions occur could provide knowledge on how charged particle populations organize, for instance, the bow shock and structure of the magnetosheath. Finally, looking at plots of ion temperature anisotropy versus parallel ion plasma beta and replacing the firehose instability threshold with the ion-cyclotron threshold would demonstrate if the ions distributions are as unstable as the electron distributions. As was mentioned in Section 4, the ions are heated much

more substantially than electrons as the solar wind crosses the bow shock. This comparison could give more understanding into the microphysics occurring in the Mars-solar wind interaction.

Data Availability Statement

The temperature and density data used in this study are available at https://zenodo.org/record/4660366#.YcJIiG-jMLb1, and the publicly released MAVEN data is available at https://pds-ppi.igpp.ucla.edu/mission/MAVEN.

Acknowledgments
We acknowledge support from the MAVEN contract and from the Solar System Workings program through Grant 80NSSC20K0571. Parts of this work for the observations obtained with the SWEA instrument are supported by the French space agency CNES.

References

Bertucci, C., Duru, F., Edberg, N., Fraenz, M., Martinecz, C., Szego, K., & Vaisberg, O. (2012). The induced magnetospheres of Mars, Venus, and Titan. In *The Plasma Environment of Venus* (Vol. 37, p. 113). https://doi.org/10.1007/978-1-4614-3290-6_5

Bouchard, C., & Carette, J. (1980). The surface potential barrier in secondary emission from semiconductors. *Surface Science*, *100*(1), 251–268. https://doi.org/10.1016/0039-6028(80)90456-2

Chew, G. F., Goldberger, M. L., & Low, F. E. (1956). The Boltzmann equation and the one-fluid hydromagnetic equations in the absence of particle collisions. *Proceedings of the Royal Society of London - Series A: Mathematical and Physical Sciences*, *236*(1204), 112–118. Retrieved from http://www.jstor.org/stable/99870

Connerney, J. E. P., Espley, J., Lawton, P., Murphy, S., Odom, J., Oliversen, R., & Sheppard, D. (2015). The MAVEN magnetic field investigation. *Space Science Reviews*, *195*(1–4), 257–291. https://doi.org/10.1007/s11214-015-0169-4

Crider, D. H., Brain, D. A., Acuña, M. H., Vignes, D., Mazelle, C., & Bertucci, C. (2004). Mars global surveyor observations of solar wind magnetic field draping around mars. *Space Science Reviews*, *111*(1), 203–221. https://doi.org/10.1023/B:SPAC.0000032714.66124.4e

Dimmock, A. P., Osmane, A., Pulkkinen, T. I., & Nykyri, K. (2015). A statistical study of the dawn-dusk asymmetry of ion temperature anisotropy and mirror mode occurrence in the terrestrial dayside magnetosheath using THEMIS data. *Journal of Geophysical Research*, *120*(7), 5489–5503. https://doi.org/10.1002/2015JA021192

Dubinin, E., Fränz, M., Woch, J., Roussos, E., Barabash, S., Lundin, R., & Acuña, M. (2007). Plasma morphology at mars. ASPERA-3 observations. In *The mars plasma environment* (p. 209). https://doi.org/10.1007/978-0-387-70943-7-8

Dubinin, E., Modolo, R., Fraenz, M., Woch, J., Duru, F., Akalin, F., et al. (2008). Structure and dynamics of the solar wind/ionosphere interface on mars: MEX-ASPERA-3 and MEX-MARSIS observations. *Geophysical Research Letters*, *35*(11), L11103. https://doi.org/10.1029/2008GL033730

Fränz, M., Dubinin, E., Roussos, E., Woch, J., Winningham, J. D., Frahm, R., et al. (2006). Plasma moments in the environment of mars. Mars express ASPERA-3 observations. *Space Science Reviews*, *126*(1–4), 165–207. https://doi.org/10.1007/s11214-006-9115-9

Gary, S. P., Lavraud, B., Thomsen, M. F., Lefebvre, B., & Schwartz, S. J. (2006). Electron anisotropy constraint in the magnetosheath: Cluster observations. In *Agu Fall Meeting Abstracts* (Vol. 2006, p. SM51C–1413).

Gary, S. P., & Nishimura, K. (2003). Resonant electron firehose instability: Particle-in-cell simulations. *Physics of Plasmas*, *10*(9), 3571–3576. https://doi.org/10.1063/1.1590982

Gary, S. P., & Wang, J. (1996). Whistler instability: Electron anisotropy upper bound. *Journal of Geophysical Research*, *101*(A5), 10749–10754. https://doi.org/10.1029/96JA00323

Halekas, J. S., Brain, D. A., Luhmann, J. G., DiBraccio, G. A., Ruhunusiri, S., Harada, Y., & Jakosky, B. M. (2017). Flows, fields, and forces in the mars-solar wind interaction. *Journal of Geophysical Research*, *122*(11), 11320–11341. https://doi.org/10.1002/2017JA024772

Halekas, J. S., Taylor, E. R., Dalton, G., Johnson, G., Curtis, D. W., McFadden, J. P., et al. (2015). The solar wind ion analyzer for MAVEN. *Space Science Reviews*, *195*(1–4), 125–151. https://doi.org/10.1007/s11214-013-0029-z

Jakosky, B. M., Lin, R. P., Grebowsky, J. M., Luhmann, J. G., Mitchell, D. F., Beutelschies, G., et al. (2015). The mars atmosphere and volatile evolution (MAVEN) mission. *Space Science Reviews*, *195*(1–4), 3–48. https://doi.org/10.1007/s11214-015-0139-x

Lavraud, B., & Larson, D. E. (2016). Correcting moments of in situ particle distribution functions for spacecraft electrostatic charging. *Journal of Geophysical Research*, *121*(9), 8462–8474. https://doi.org/10.1002/2016JA022591

Lu, Q., Shan, L., Shen, C., Zhang, T., Li, Y., & Wang, S. (2011). Velocity distributions of superthermal electrons fitted with a power law function in the magnetosheath: Cluster observations. *Journal of Geophysical Research*, *116*(A3), A03224. https://doi.org/10.1029/2010JA016118

Masood, W., & Schwartz, S. J. (2008). Observations of the development of electron temperature anisotropies in Earth's magnetosheath. *Journal of Geophysical Research*, *113*(A1), A01216. https://doi.org/10.1029/2007JA012715

Mazelle, C. X., Meziane, K., Mitchell, D. L., Garnier, P., Espley, J. R., Hamza, A. M., et al. (2018). Evidence for neutrals-foreshock electrons impact at mars. *Geophysical Research Letters*, *45*(9), 3768–3774. https://doi.org/10.1002/2018gl077298

Mazelle, C., Winterhalter, D., Sauer, K., Trotignon, J. G., Acuña, M. H., Baumgärtel, K., & Slavin, J. (2004). Bow shock and upstream phenomena at mars. *Space Science Reviews*, *111*(1), 115–181. https://doi.org/10.1023/B:SPAC.0000032717.98679.d0

McFadden, J. P., Carlson, C. W., Larson, D., Bonnell, J., Mozer, F., Angelopoulos, V., et al. (2008). THEMIS ESA first science results and performance issues. *Space Science Reviews*, *141*(1–4), 477–508. https://doi.org/10.1007/s11214-008-9433-1

Mitchell, D. L., Mazelle, C., Sauvaud, J. A., Thocaven, J. J., Rouzaud, J., Fedorov, A., et al. (2016). The MAVEN solar wind electron analyzer. *Space Science Reviews*, *200*(1–4), 495–528. https://doi.org/10.1007/s11214-015-0232-1

Mitchell, J. J., & Schwartz, S. J. (2014). Isothermal magnetosheath electrons due to nonlocal electron cross talk. *Journal of Geophysical Research*, *119*(2), 1080–1093. https://doi.org/10.1002/2013JA019211

Moses, S. L., Coroniti, F. V., & Scarf, F. L. (1988). Expectations for the microphysics of the Mars-solar wind interaction. *Geophysical Research Letters*, *15*(5), 429–432. https://doi.org/10.1029/GL015i005p00429

Ruhunusiri, S., Halekas, J. S., Espley, J. R., Eparvier, F., Brain, D., Mazelle, C., et al. (2018). One-hertz waves at mars: MAVEN observations. *Journal of Geophysical Research*, *123*(5), 3460–3476. https://doi.org/10.1029/2017JA024618

Scholtz, J., Dijkkamp, D., & Schmitz, R. (1996). Secondary electron emission properties. *Philips Journal of Research*, *50*(3), 375–389. https://doi.org/10.1016/S0165-5817(97)84681-5

Schwartz, S. J., Andersson, L., Xu, S., Mitchell, D. L., Akbari, H., Ergun, R. E., & Meziane, K. (2019). Collisionless electron dynamics in the magnetosheath of mars. *Geophysical Research Letters*, *46*(21), 11679–11688. https://doi.org/10.1029/2019GL085037

Štverák, Š., Trávníček, P., Maksimovic, M., Marsch, E., Fazakerley, A. N., & Scime, E. E. (2008). Electron temperature anisotropy constraints in the solar wind. *Journal of Geophysical Research*, *113*(A3), A03103. https://doi.org/10.1029/2007JA012733

Wang, C.-P., Gkioulidou, M., Lyons, L. R., & Angelopoulos, V. (2012). Spatial distributions of the ion to electron temperature ratio in the magnetosheath and plasma sheet. *Journal of Geophysical Research*, *117*(A8), A08215. https://doi.org/10.1029/2012JA017658

Xu, S., Schwartz, S. J., Mitchell, D. L., Horaites, K., Andersson, L., Halekas, J., et al. (2021). Cross-shock electrostatic potentials at mars inferred from MAVEN measurements. *Journal of Geophysical Research: Space Physics*, *126*(3). https://doi.org/10.1029/2020ja029064